ACS NANO

www.acsnano.org

ARTICLE

Catalytic Metasurfaces Empowered by Bound States in the Continuum

Haiyang Hu, Thomas Weber, Oliver Bienek, Alwin Wester, Ludwig Hüttenhofer, Ian D. Sharp, Stefan A. Maier, Andreas Tittl,* and Emiliano Cortés

Cite This: *ACS Nano* 2022, 16, 13057−13068

Read Online

ACCESS | Metrics & More | Article Recommendations | Supporting Information

ABSTRACT: **Photocatalytic platforms based on ultrathin reactive materials facilitate carrier transport and extraction but are typically restricted to a narrow set of materials and spectral operating ranges due to limited absorption and poor energy-tuning possibilities. Metasurfaces, a class of 2D artificial materials based on the electromagnetic design of nanophotonic resonators, allow optical absorption engineering for a wide range of materials. Moreover, tailored resonances in nanostructured materials enable strong absorption enhancement and thus carrier multiplication. Here, we develop an ultrathin catalytic metasurface platform that leverages the combination of loss-engineered substoichiometric titanium oxide (TiO_{2-x}) and the emerging physical concept of optical bound states in the continuum (BICs) to boost photocatalytic activity and provide broad spectral tunability. We demonstrate that our platform reaches the condition of critical light coupling in a TiO_{2-x} BIC metasurface, thus providing a general framework for maximizing light−matter interactions in diverse photocatalytic materials. This approach can avoid the long-standing drawbacks of many naturally occurring semiconductor-based ultrathin films applied in photocatalysis, such as poor spectral tunability and limited absorption manipulation. Our results are broadly applicable to fields beyond photocatalysis, including photovoltaics and photodetectors.**

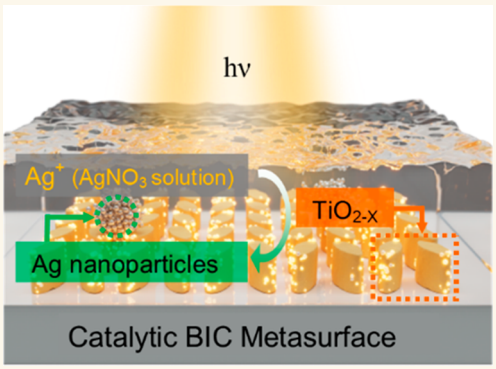

KEYWORDS: *nanophotonics, metasurfaces, titanium dioxide, bound states in the continuum, photocatalysis, critical coupling*

Photocatalytic platforms and devices based on ultrathin films are highly desirable because they offer dramatic enhancements to photocarrier excitation and enable facile short-range carrier transport, but they are often limited by insufficient light absorption.[1,2] Increasing the thickness of the semiconductor above the penetration depth of light ensures maximum optical absorption, but it can hinder the efficient utilization of the captured energy due to bulk recombination. Hence, obtaining strong light absorption in ultrathin semiconductors has been of great scientific and technological interest for many years, making it one of the essential aspects for the efficient generation of photocarriers, as well as the development of ultrafast optoelectronic devices[3−5] and surface-active photocatalysts.[6,7] However, ultrathin films of many naturally occurring semiconductor materials provide only limited freedom for controlling the spectral location and magnitude of light absorption, since their intrinsic optical properties are fixed.[2] In contrast, ultrathin metasurfaces constructed from two-dimensional subwavelength arrays of semiconductor structures have shown tremendous potential for concentrating and controlling light on the nanoscale, positioning them as an ideal toolkit for engineering the light absorption in catalytic materials.[8−20] Indeed, recent examples have shown that such artificial materials can increase the internal quantum efficiency of semiconductors and metals when shaping them into catalytic metasurfaces.[13,14]

All-dielectric metasurfaces underpinned by the physics of bound states in the continuum (BIC) have seen surging interest due to their spectral selectivity, strong light confinement, and giant enhancement of electromagnetic fields,[21−29] sparking applications in diverse fields including nanoscale lasing,[30−36] biomolecular sensing,[37−40] and nonlinear photonics.[41−44] However, to the best of our knowledge, BICs have not yet been tailored for photocatalytic applications. Conceptually, a BIC is a localized state existing at the same energy level as a continuum of radiation modes.[45] This

Received: June 9, 2022
Accepted: July 26, 2022
Published: August 11, 2022

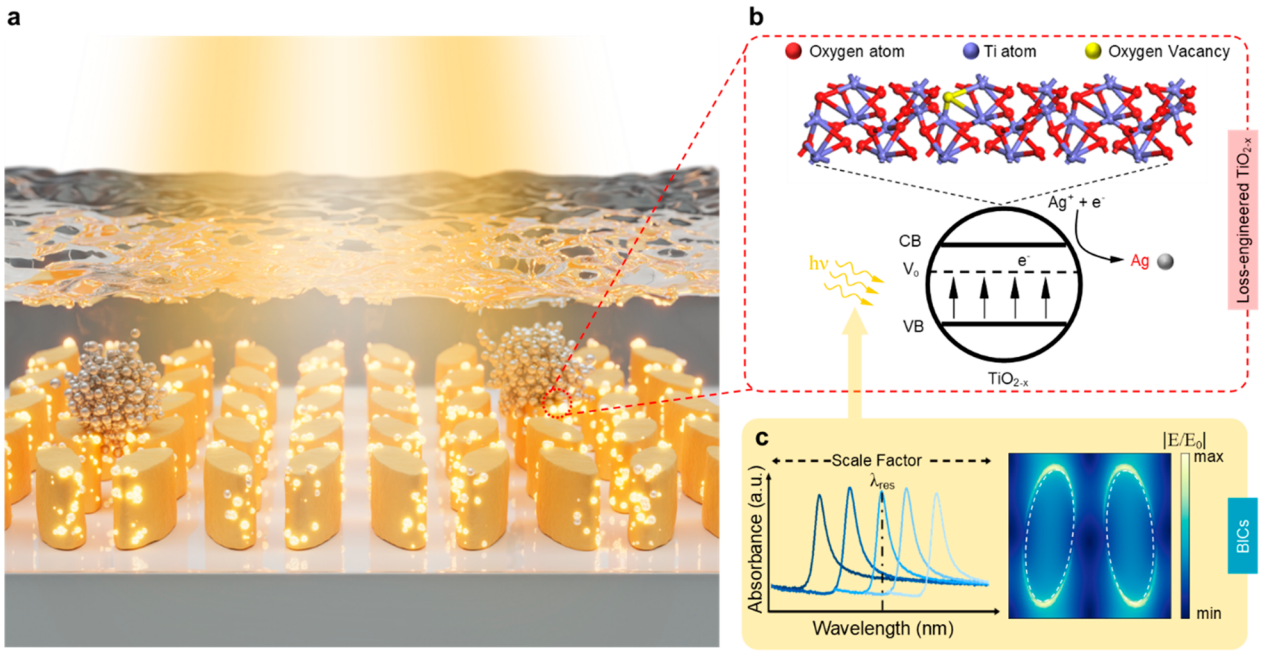

Figure 1. Catalytic metasurfaces driven by bound states in the continuum. (a) Schematic of the TiO_{2-x}-based BIC metasurface platform for the photoreduction of silver ions, where reduced silver particles aggregate on the surface, revealing the active sites and overall functionality of the platform. (b) Schematic of oxygen vacancies acting as the defect energy level between the conduction band and valence band, which extends the light absorption to the visible region. The photoexcited electron exhibits strong reducing reactivity, resulting in the reduction of Ag^+ ions. (c) The reduction rate of Ag^+ is increased via metasurface-enhanced light absorption at a given excitation wavelength. Spectral tunability of the catalytic metasurfaces is achieved by adjusting the scaling factor of the unit cell, which enables versatile control over the resonance position throughout the visible spectrum (left). Strong nanoscale light confinement and enhancement of the local electromagnetic fields of the catalytic metasurface are provided by the BIC concept (right). This idea can be extended to other materials.

phenomenon originally appeared in quantum mechanics and has later been applied to many other areas of physics.[46] A true BIC with an infinite value of the quality factor (Q factor, defined as the resonance position divided by the line width) can only exist as a mathematical object and can be explained by vanishing coupling constants with all radiation channels. One way of making BICs usable for practical nanophotonics systems is to leverage symmetry-protected metasurfaces, where the coupling constants are tailored using structural asymmetry within the metasurface unit cell, leading to the formation of quasi-BIC modes accessible from the far-field.[21] A central advantage of symmetry-protected BICs is their ability to provide precise control over the resonance properties (and, specifically, the Q factor) through a straightforward geometrical tuning parameter, making them ideal for tailoring light−matter interactions. However, extending these ideas into the field of photocatalysis, where they could enable ways of triggering chemical transformations with light, has so far not been investigated.

Established BIC-based metasurface demonstrations have utilized high refractive index materials like Si,[47,48] where pushing the operating range toward the blue part of the visible spectrum is still challenging due to significant dielectric losses associated with the interband transitions.[49] The blue side of the optical regime is particularly interesting for catalysis because the band gap and band alignment of many relevant semiconductors lie in the 2−3 eV region and because the energy of (hot) electron−hole pairs in metals is in most cases high enough for promoting hydrogen generation or oxygen evolution, among other important chemical transformations. In particular, TiO_2 is a promising alternative to Si because of its extremely low losses throughout the visible wavelength range (400−750 nm), but it has, so far, not been employed in the context of two-dimensional BIC-based systems. In addition, TiO_2 is an ideal photocatalyst with advantages like chemical stability, band alignment with the water-splitting reaction, nontoxicity, and long-term durability, enabling the efficient conversion of solar into chemical energy.[50] The photocatalytic properties of TiO_2 are derived from photogenerated charge carriers (holes and electrons), which transfer to the surface and participate in reduction or oxidation processes.[51] In this way, the energy of photons can be stored in chemical bonds, which has stimulated many TiO_2-based photocatalytic applications like hydrogen fuel production and pollutant degradation.[51] Importantly, the extinction coefficient k of TiO_2 can be tuned throughout the visible spectrum by introducing oxygen vacancies (leading to the formation of oxygen-vacancy-rich TiO_2 or TiO_{2-x}),[15,52−56] which provide a strong potential for absorption engineering when combined with nanophotonic concepts such as BICs.

Here, we engineer catalytic TiO_{2-x} based BIC metasurfaces to provide strong light confinement and flexible absorption control for visible-light photocatalysis (Figure 1). We use a standard Ag reduction reaction[15,52] to reveal the active sites on the metasurface and find a significant increase in the reduction rate of a factor ∼7 compared to nonresonant structures. This finding highlights the potential of this strategy to circumvent the intrinsic trade-off between light absorption and photocarrier recombination on ultrathin photocatalytic films. We show that strong electromagnetic near-fields within the semiconductor material are crucial for the enhancement of such processes, providing guidelines for boosting light−matter interactions and photocatalytic activity.[13,15,53,54] Furthermore, we find that strong near-fields are readily achieved in

https://doi.org/10.1021/acsnano.2c05680
ACS Nano 2022, 16, 13057−13068

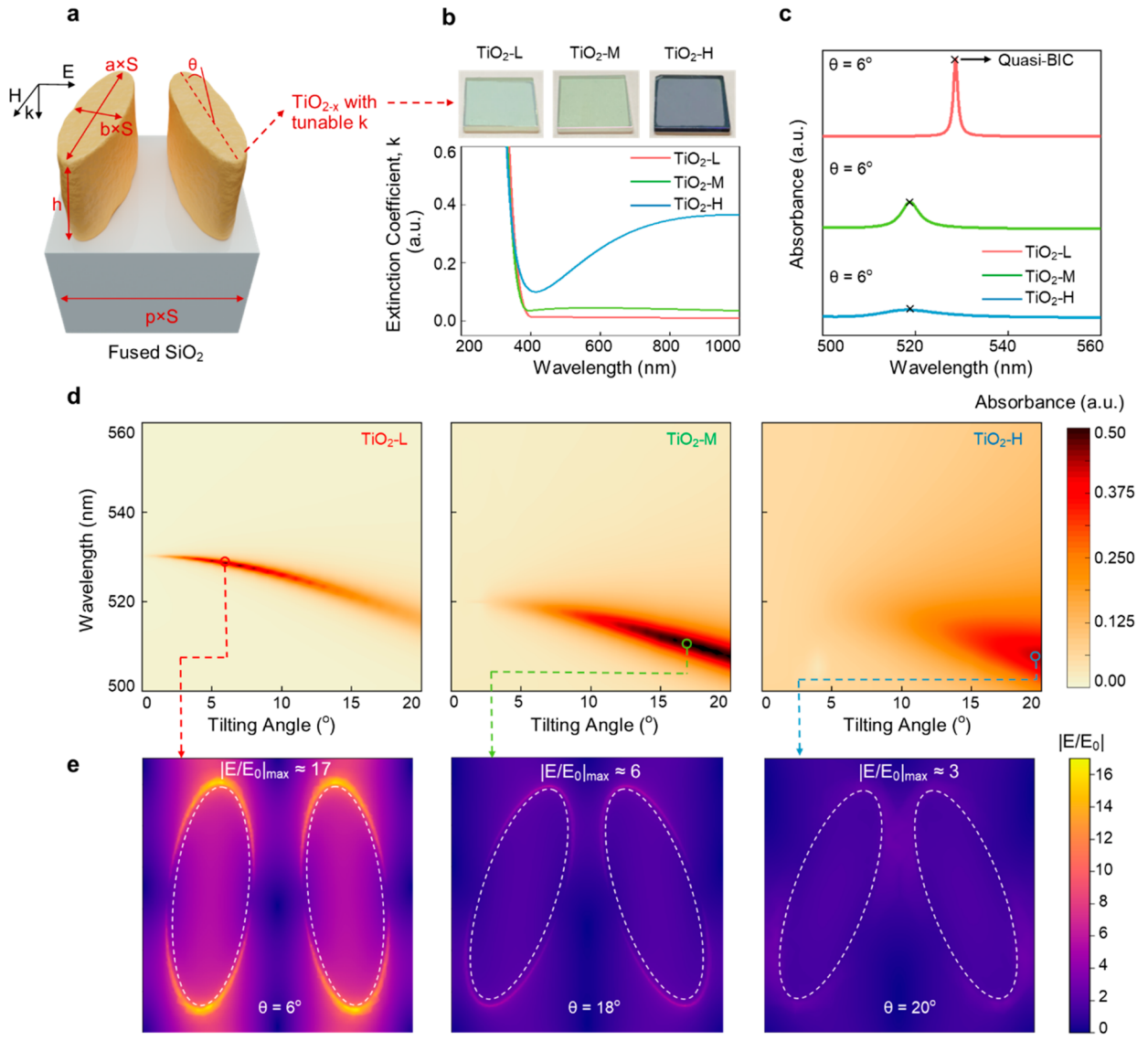

Figure 2. Numerical design of the catalytic metasurfaces. (a) Sketch of a TiO_{2-x} BIC unit cell (scaling factor $S = 1$) with tunable extinction coefficient k and tilting angle θ. The geometrical parameters of the unit cell are $a = 274$ nm, $b = 103$ nm, $h = 100$ nm, and $p = 331$ nm, where the parameters a, b, and p are scaled linearly with S. (b) Photographs and spectrally resolved extinction coefficients of TiO_{2-x} films (deposited on SiO_2) with different extinction coefficients k prepared by atomic layer deposition (ALD). TiO_{2-x} films are denoted as TiO_2-L, TiO_2-M, and TiO_2-H for the lowest, moderate, and highest oxygen vacancy concentrations, respectively. (c) Simulated absorbance spectra of BIC metasurfaces with $S = 1$ composed of different TiO_{2-x} materials (TiO_2-L, TiO_2-M, and TiO_2-H) with a tilting angle of $\theta = 6°$. In this visible region, the real part of the complex relative permittivity of TiO_2-L is approximately 6.4, while the values for TiO_2-M and TiO_2-H are both approximately 5.8. (d) Color-coded simulated absorbance maps of the different catalytic metasurfaces as a function of tilting angle θ and wavelength λ. (e) Electric near-fields (taken at $h = 0$) of individual unit cells of the different TiO_2-L, TiO_2-M, and TiO_2-H metasurfaces with the respective optimal tilting angles ($\theta = 6$, 18, and 20°) corresponding to maximum absorption enhancement.

metasurfaces composed of TiO_{2-x} with low extinction coefficient through precise matching of intrinsic and radiative losses (i.e., by utilizing BICs with narrow line widths). This brings another dimension for the field of photocatalysis, where the use of semiconductors with high extinction coefficients is usually preferred. Additionally, we extend the understanding of light−matter coupling in our BIC-enabled systems to materials with different extinction coefficients based on temporal coupled-mode theory, which provides a general framework for maximizing light−matter interactions in diverse heavily used photocatalytic materials like ZnO, SnO_2, SiC, and others. BIC-based metasurfaces can thus efficiently utilize typically poor light-absorbing materials and enable their use for the realization of versatile and selectively absorbing nanophotonic systems.

RESULTS AND DISCUSSION

Numerical Design of Catalytic BIC Metasurfaces. As a basis for our TiO_{2-x}-based BIC metasurface platform, we utilize a unit cell composed of two elliptical resonators on a silicon dioxide substrate (Figure 2a). Compared to other BIC unit cell geometries, the two ellipse structure exhibits the strongest fabrication robustness[57] and maintains its volume when breaking the symmetry using the ellipse tilting angle, which is important for comparing of photo reduction rate between metasurfaces with different asymmetry factors.

https://doi.org/10.1021/acsnano.2c05680
ACS Nano 2022, 16, 13057−13068

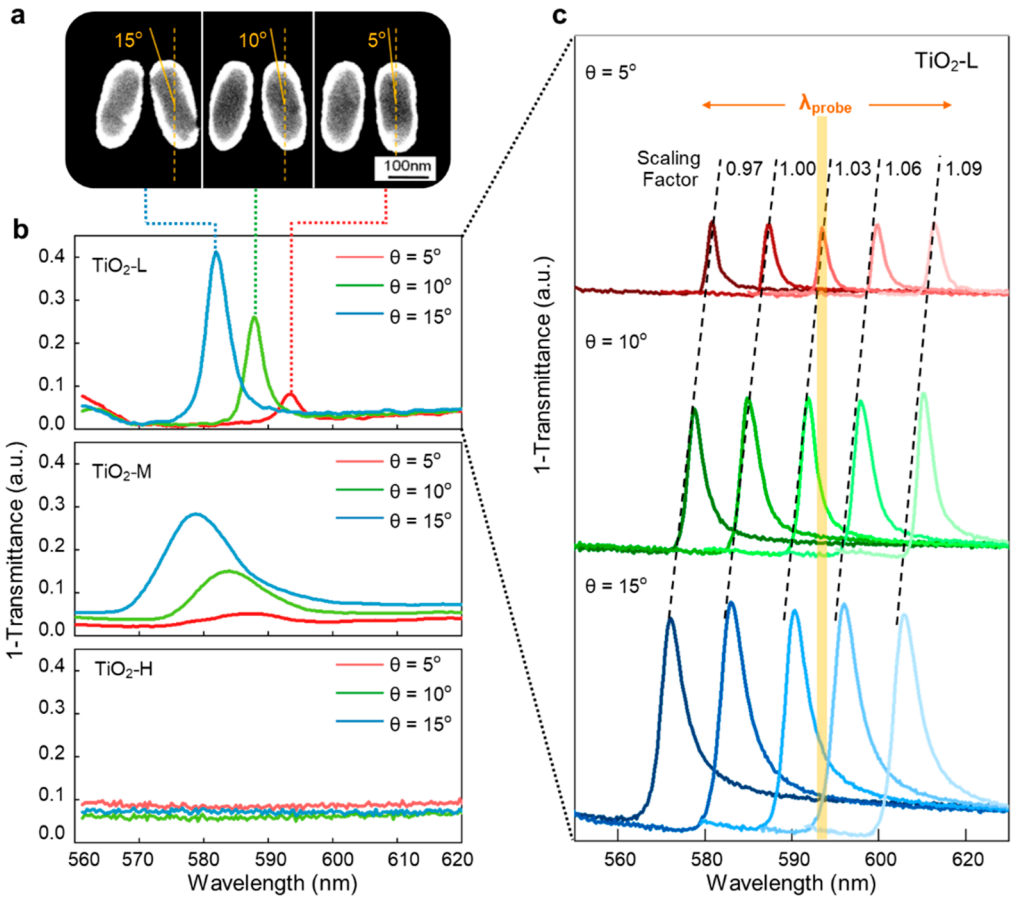

Figure 3. Experimental metasurface realization and spectral tuning. (a) SEM images of exemplary two ellipse metasurface unit cells (scaling factor $S = 1$) with different tilting angle values of 5, 10, and 15°. (b) Measured 1-transmittance spectra for metasurfaces with different tilting angles (θ = 5, 10, and 15°) and different defect concentrations of the TiO_2 films (TiO_2-L, TiO_2-M, and TiO_2-H). (c) Measured 1-transmittance spectra for low-defect TiO_2-L metasurfaces with unit cells of different scaling factors S and tilting angles θ.

As introduced above, a true BIC is a mathematical concept with an infinite quality factor and vanishing spectral line width. In practice, BICs can be converted to quasi-BICs with finite resonance width once the in-plane inversion symmetry of the unit cell is broken, enabling the excitation of the resonant mode from the far-field. In our case, this symmetry breaking is induced by tilting the ellipses under an angle θ with respect to each other. We implement titanium oxide layers with three different concentrations of oxygen vacancies, characterized by varying extinction coefficients k (in the visible region), which are denoted as TiO_2-L ($k \approx 0.003$), TiO_2-M ($k \approx 0.022$), and TiO_2-H ($k \approx 0.110$) for the lowest, moderate, and the highest Vo concentration, respectively (Figure 2b). Exact dielectric functions for the three films were determined with spectral ellipsometry and used as input for our numerical metasurface design process. The tunable defect concentration can be realized during atomic layer deposition (ALD) by choosing different precursors (see the "Methods" section). Such defects can influence both the electromagnetic properties of the material (by regulating the losses and absorption) and the reactivity (by altering the dynamics of the photogenerated electron–hole pairs).[58−62] In order to identify the optimal TiO_{2-x}-based BIC metasurface design for photocatalysis, we will consider both the optical and catalytic properties of the system.

On the basis of our simulations, for the low-defect case (TiO_2-L), a sharp quasi-BIC resonance can be obtained in the metasurface absorbance spectrum ($A = 1 - R - T$), where maximum visible light absorption at a wavelength of 530 nm occurs for an asymmetry parameter of $\theta = 6°$ (Figure 2c). With the same metaunit geometry and asymmetry parameter, metasurfaces realized with TiO_2-M and TiO_2-H show reduced resonance-assisted absorption and exhibit significantly broadened resonance line shapes. This absorption reduction originates from the damping of the metasurface resonance by the intrinsic loss of the materials, as quantified by the extinction coefficient (k), and it contrasts with the behavior in unstructured thin films, where increased absorption is expected for higher defect concentrations. The complex interplay between material loss and resonant absorption highlights the need for tailoring the metasurface design to specific material parameters.

To provide a deeper understanding of the metasurface-enhanced light–matter interaction, we have examined the variation of the resonant absorption with the asymmetry parameter θ for all given values of the intrinsic material loss k (Figure 2d). As discussed above, we find that the absorption in regions of the parameter space away from the resonance (where no metasurface-based enhancement occurs) increases with the extinction coefficient (k), as illustrated by the overall darker color in simulated absorbance maps of the TiO_2-M and TiO_2-H metasurfaces compared to TiO_2-L. Introduction of the quasi-BIC resonance greatly boosts light confinement and optical absorption compared to the off-resonant case. For the

https://doi.org/10.1021/acsnano.2c05680
ACS Nano 2022, 16, 13057−13068

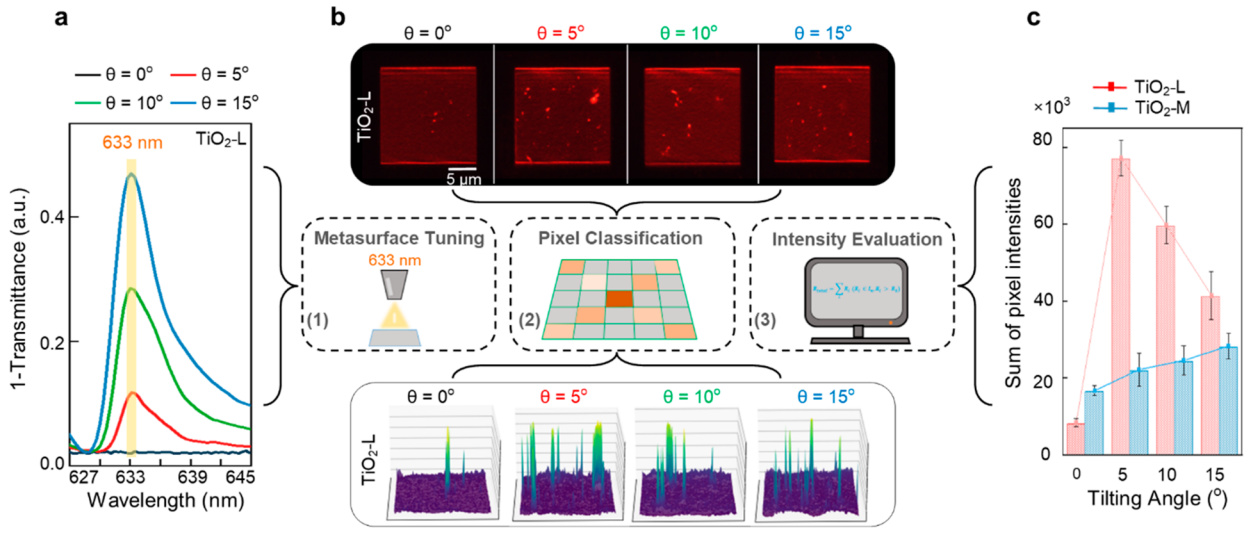

Figure 4. Evaluation of catalytic metasurface performance. (a) 1-Transmittance spectrum measured in an aqueous environment for metasurfaces with tilting angles θ = 0, 5, 10, and 15° based on TiO_2-L, where the scaling factors of unit cells are finely adjusted to place the quasi-BICs resonances at the target wavelength position (633 nm). (b) Dark-field images (top) illustrate different visible-light photocatalytic reduction rates on the metasurfaces with different tilting angles (θ = 0, 5, 10, and 15°) based on TiO_2-L. The nonresonant metasurface pattern (θ = 0°) is used for comparison because it maintains the same volume, material mass, and active surface area as the BIC-driven systems. The photocatalytic experiments were performed in $AgNO_3$ solution (50 mM) and illuminated with the focused CW laser from the top (633 nm, 50 mW). To enable observation of the reduction process, an additional broadband light source was used for dark-field illumination. To avoid the excitation of TiO_2 by UV light from the broadband source, a long-pass filter (590 nm) was applied, causing the reddish appearance of the dark-field images. The bright red spots are reduced Ag particles aggregated on the metasurfaces. Signal locations and intensities associated with Ag nanoparticles on planar images are visualized in 3D models (bottom), where the intensity of red pixels is represented by the height as a function of the spatial position. (c) On the basis of the digital image analysis in panel b for each metasurface, the sum of red light intensity enables direct comparison of the different Ag^+ reduction rates on metasurfaces as a function of their tilting angles.

low-defect material (TiO_2-L), a clear region of the parameter space with optimal absorption can be identified, with a maximum for θ = 6°. Similar regions of optimal absorption are present for the medium- and high-defect cases as well, but these show broader line widths and are found for higher asymmetry parameters (θ = 18 and 20° for TiO_2-M and TiO_2-L, respectively), indicating a systematic connection between the metasurface and material properties. In addition to the absorbance spectrum, the total optical power absorbed by the TiO_{2-x} ellipses (i.e., the volume loss) exhibits the same trend (Figure S1). To describe the coupling of incident light with the catalytic metasurfaces from an analytical perspective, we will provide a detailed discussion based on temporal coupled-mode theory (TCMT) in the "BIC-Enabled Critical Light–Matter Coupling" section.

Even though the metasurface designs for the different materials share similar values of maximum absorption for their optimum asymmetry parameters, their electromagnetic near-field patterns differ greatly. Specifically, the maximum electric field enhancement ($|E/E_0|_{max}$) in the hot spots of the TiO_2-L metasurface (i.e., at the tips of the ellipsoids) is around 3 times higher than that of TiO_2-M and 6 times higher than that of TiO_2-H (Figure 2e), which means that the light–matter interaction is much more intense in TiO_2-L than in the other cases, demonstrating the importance of efficient resonant enhancement for obtaining maximum absorption. Advantageously, the near-field enhancement of our structures does not strongly depend on the resonator height (Figure S2). Our simulations highlight the capabilities of BIC-based metasurfaces for engineering visible-light absorption and strong nanoscale light confinement at the catalytic TiO_{2-x} interface.

Experimental Realization of TiO_{2-x}-Based Metasurfaces. The TiO_{2-x}-based metasurfaces were realized using a top-down nanofabrication process based on high-resolution electron beam lithography and anisotropic reactive ion etching (see the "Methods" section). Intentionally lossy TiO_{2-x} thin films with a thickness of 100 nm were fabricated by atomic layer deposition (ALD), and their extinction coefficients were engineered by choosing different metalorganic precursors, tetrakis(dimethylamino) titanium (TDMAT) and titanium isopropoxide (TTIP), combined with either thermal (H_2O) or plasma-enhanced (O_2) oxidation steps (see the "Methods" section). We experimentally realized metasurface designs with asymmetry parameters of θ = 5, 10, and 15° for all three defect concentrations (TiO_2-L, TiO_2-M, and TiO_2-H) and verified their accurate reproduction using scanning electron microscopy (SEM, see Figure 3a). The specific values of the asymmetry parameters, though slightly different from the numerically predicted optimum values, were chosen for better reproducibility and stability within the constraints of our nanofabrication processes. Nevertheless, it is important to note that the experimentally realized asymmetry values span a sufficient range to clearly elucidate the different light–matter coupling regimes (see the "BIC-Enabled Critical Light–Matter Coupling" section).

The presence of quasi-BIC resonances for the TiO_2-L and TiO_2-M cases was confirmed through white light transmittance measurements (see the "Methods" section), and a clear blueshift of the resonance wavelength with increasing θ was observed, consistent with the numerical predictions (Figure 3b). Notably, no resonance was observed for the highest defect concentration material, TiO_2-H, which we attribute to the

https://doi.org/10.1021/acsnano.2c05680
ACS Nano 2022, 16, 13057–13068

signal-to-noise characteristics of our optical spectroscopy setup considering the already very weak resonance expected from simulations (compare Figure 2c). We find that the quality factor of the metasurfaces is clearly correlated with the asymmetry parameter, showing a gradual decrease with increasing θ. As expected, the Q factors of the TiO_2-L metasurfaces are much higher than those composed of TiO_2-M with the same θ (Figure S3). Because of the extremely weak and broad resonances observed for TiO_2-H, we focus our catalytic experiments on metasurfaces fabricated from TiO_2-L and TiO_2-M, which nevertheless provide a broad range of resonance Q factors and absorption efficiencies for analysis.

We experimentally demonstrate the spectral tunability of the catalytic metasurfaces through tuning the scaling factor S of the unit cell, which enables versatile control over the resonance position throughout the visible spectrum. Transmittance measurements confirm that the positions of quasi-BIC resonances can be precisely placed at a given excitation wavelength through tailoring the scaling factors (Figure 3c), providing flexibility to create BIC-induced absorption enhancement at any desired wavelength in the visible region.

Metasurface-Enhanced Photocatalysis. We use a standard Ag reduction reaction[15,52] to investigate the potential of TiO_{2-x}-based BIC metasurfaces as a functional photocatalysis platform (Figure S4). A red CW laser source with an emission wavelength of 633 nm was used to trigger the photoreduction process. Fine tuning of the scaling factor of the unit cell was carried out to place the quasi-BIC resonance at the target excitation wavelength of 633 nm for all asymmetry parameters, taking into account the slight resonance shifts caused by a variation of θ (see Figure 2d). Transmittance spectra measured in an aqueous environment confirm that the resonances of different TiO_2-L and TiO_2-M metasurfaces can be excited at 633 nm (Figures 4a and S5). To investigate the visible-light photocatalytic performance of our BIC-based metasurfaces, the photoreduction of silver ions was conducted for samples with different asymmetry parameters (θ = 0, 5, 10, and 15°). The metasurface samples were immersed in 50 mM silver nitrate ($AgNO_3$) aqueous solution, and a CW laser (633 nm, 50 mW) was used to illuminate the target metasurface area. When illuminated, the excited electrons created in the TiO_{2-x} transfer to Ag^+, resulting in the generation of Ag nanoparticles on the metasurfaces.[15,52] Additionally, with the aid of the metasurface resonance, the absorption of light at the electric field hot spots is enhanced considerably, which boosts the charge carrier excitation and thus, reduction rate. The photogenerated holes are consumed by hydroxide to generate oxygen and water, which ensures the reduction reaction can further proceed.[63,64]

Visible-light photocatalysis can be monitored through dark-field microscopy by tracking the amount of Ag particles created on the surface, which manifest as distinct bright red spots accumulating in the dark-field images over time (Figure 4b). Therefore, through analysis of the brightness and size of these characteristic spots, we can provide an estimation of the amount of reduced Ag nanoparticles, which is related to the photocatalytic rate on the different metasurface fields. We note that the Ag particles are not generated evenly on the metasurface, because the growth is influenced by the local surface environment, including effects such as the local availability of active sites, adsorption energy, and initial Ag seed deposition. Similar distributions of Ag particles on TiO_2 nanostructures have been reported before.[15,52]

To quantify the amount of Ag reduced at the metasurface, a statistical approach was employed based on the distribution and brightness of the red pixels in the captured dark-field images. The locations and intensity of the signals induced by the Ag particles are visualized in three dimensions in Figure 4b, where the intensity of the red pixels is represented by the height of the peaks. By applying thresholding, the signals of the Ag particles can be separated from the background, and a sum of pixel intensities can be calculated to estimate the photoreduction rate (see the "Methods" section). The results of the numerical image analysis for different metasurfaces are shown in Figure 4c for metasurface structures composed of TiO_2-L and TiO_2-M.

The BIC metasurface concept allows us to completely turn off the resonant enhancement by moving to a fully symmetric unit cell design, which provides an ideal reference case for our analysis of the photocatalytic rates. For a symmetric metasurface (θ = 0°) composed of TiO_2-L, we find an extremely low Ag^+ photoreduction rate at 633 nm, which we attribute to the low intrinsic absorption of the material caused by a small number of defects. The nonresonant reduction rate of TiO_2-M is around 2 times higher (Figure 4c) than that of TiO_2-L, which is expected considering the difference in extinction coefficient between the two materials (see Figure 2b).

This picture changes drastically when moving to the resonantly enhanced case. Notably, for the TiO_2-L metasurface with an asymmetry parameter of θ = 5°, the reduction rate (as evaluated by our image processing approach) is boosted by a factor of 7, providing the greatest enhancement of quasi-BIC-assisted light absorption compared to the other metasurface geometries (θ = 10 and 15°), as predicted by our simulations. The quantities of deposited Ag and therefore the reduction rates are closely related to the capability of the different metasurface samples to absorb visible light.[15]

Notably, the metasurface-enhanced reduction rate on TiO_2-M is lower than that of TiO_2-L for all asymmetries (θ = 5, 10, and 15°), which is due to the weaker resonances in TiO_2-M as well as the associated lower quality factors and electric field enhancements. This resonance attenuation is driven by the higher extinction coefficient of TiO_2-M compared to TiO_2-L and leads to overall weaker light−matter interaction in the photoreduction process. Nevertheless, the TiO_2-M metasurface geometries still allow an asymmetry-dependent assessment of the BIC-enhanced photoreduction rate, which shows a maximum for θ = 15°, consistent with the numerical simulations. In order to understand why maximum absorption occurs at markedly different asymmetry parameters for the different materials (θ = 5° for TiO_2-L and θ = 15° for TiO_2-M), a fundamental model for light−matter interactions in BIC-based metasurfaces is necessary, which we develop in the following section.

Strikingly and in contrast to typical photocatalysis platforms where materials with high extinction coefficient are preferred, BIC-based metasurfaces incorporating low-defect TiO_2-L exhibit much higher catalytic performance as well as greater flexibility for optical absorption engineering through tuning of the asymmetry factor of the unit cell, enabling the simultaneous optimization of visible-light absorption and near-field enhancement. Therefore, our approach can enhance visible-light photocatalysis on ultrathin films, especially when utilizing weakly absorbing materials.

BIC-Enabled Critical Light−Matter Coupling. Our numerical simulations (Figure 2d) and photoreduction experi-

https://doi.org/10.1021/acsnano.2c05680
ACS Nano 2022, 16, 13057−13068

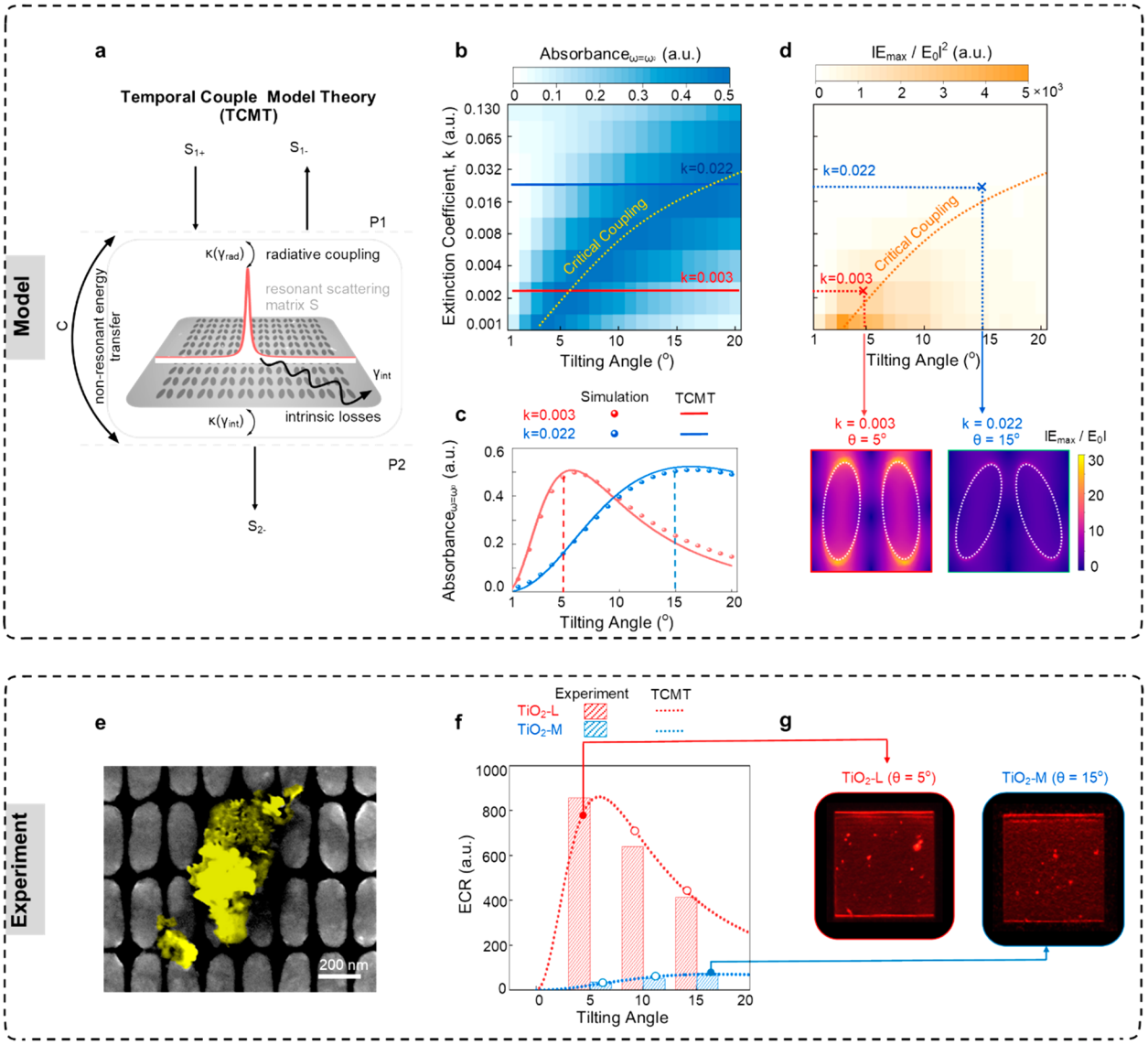

Figure 5. Critical light−matter coupling in catalytic metasurfaces. (a) Model of a metasurface with two radiative decay channels, which is illuminated from above. $s_{1/2,\pm}$ refer to the in- and outgoing waves at ports 1 and 2, γ_{rad} and γ_{int} are the radiative and intrinsic damping rates of the resonance, and κ is the coupling rate to the far-field. (b) Simulations of maximum absorbance ($\omega = \omega_0$) of metasurfaces as a function of extinction coefficient (k) and tilting angle (θ). ω_0 is the resonance frequency of the quasi-BIC. The critical coupling condition is indicated by a dotted line. (c) CST simulations with TCMT fits: the absorbance at resonance ($\omega=\omega_0$) of metasurfaces with different tilting angles (θ = 1−20°) based on the TiO_{2-x} film with different extinction coefficients (k = 0.003 and 0.022, respectively). (d) Top: Simulations of maximum field enhancement of metasurfaces as a function of extinction coefficient (k) and tilting angle (θ). Bottom: Simulation of the electric field enhancement in one unit cell (θ = 5 and 15°) based on TiO_{2-x} films with different extinction coefficients. (e) SEM images of the TiO_2-L metasurface (θ = 5°) after Ag^+ reduction. The yellow patterns are the reduced Ag particles aggregating together. (f) Normalized reduction rate ($\frac{R_{\theta,k} - R_{\theta=0,k}}{R_{\theta=0,k}}$, θ = 0, 5, 10, and 15°) based on the sum of pixel intensities shown in Figure 4c with TCMT fits, which are based on the combination of maximum absorption and field enhancement. (g) Dark-field images illustrating different photocatalytic reduction rates on the TiO_2-L metasurface (θ = 5°) and TiO_2-M metasurface (θ = 15°).

ments (Figure 4c) clearly demonstrate that to obtain maximum absorption and the highest photoreduction performance, TiO_{2-x} films with different extinction coefficients k require metasurface designs with different optimized asymmetry parameters θ. To deepen our understanding of this phenomenon, we analyze the absorption and field enhancement over a wide parameter space of extinction coefficients k and asymmetry parameters θ using temporal coupled-mode theory (TCMT).[65−67]

The BIC-enabled catalytic metasurface platform can be described as a single-mode cavity with two mirror-symmetric ports (Ports 1 and 2, see Figure 5a), which is illuminated from one side with a time harmonic excitation (s_{1+}) and allows for reflected (s_{1-}) and transmitted (s_{2-}) waves. The interaction between the far-field and the cavity mode at each port is determined by a coupling rate κ, which can be calculated from the radiative decay rate γ_{rad} via $\kappa = \sqrt{\gamma_{rad}}$. Additionally, an intrinsic decay rate γ_{int} describes the energy loss through material absorption. The far-field absorbance can then be calculated according to (see the Supporting Information)

https://doi.org/10.1021/acsnano.2c05680
ACS Nano 2022, 16, 13057−13068

$$A = \frac{2\gamma_{int}\gamma_{rad}}{(\gamma_{int} + \gamma_{rad})^2} \quad (1)$$

which has its maximum value for $\gamma_{int} = \gamma_{rad}$, referred to as the critical coupling condition.[44]

A similar critical coupling condition can be derived for the near-fields, where the electric near-field enhancement $|E/E_0|^2$ can be related to the total quality factor $Q = \omega_0/2(\gamma_{int} + \gamma_{rad})$ and the far-field absorbance A via

$$|E/E_0|^2 \sim \frac{\gamma_{rad}}{(\gamma_{int} + \gamma_{rad})^2} = \frac{4\gamma_{rad}}{\omega_0^2}\cdot Q^2 = \frac{A}{2\gamma_{int}} \quad (2)$$

A central advantage of BIC-based metasurface approaches is the precise control over the radiative decay rate via the asymmetry factor of the specific BIC unit cell design, where the relationship between γ_{rad} and α follows the characteristic quadratic relationship:[22]

$$\gamma_{rad} \sim \alpha^2 = \sin^2\theta \quad (3)$$

Additionally, the intrinsic decay rate γ_{int} follows a linear relation to k. To reveal the correlation between k, θ, and the efficiency of light−matter coupling, we simulate the far-field absorbance at resonance for different values of the extinction coefficient (k = 0.001−0.13) and tilting angle (θ = 1−20°). Notably, the maximum absorbance of A = 0.5 is reached at the critical coupling condition, indicated by a dotted line in Figure 5b. Furthermore, we fit the absorbance data corresponding to the two extinction values of our experimental TiO_2-L and TiO_2-M films (i.e., k = 0.003 and 0.022) with eq 2, which shows excellent agreement between our model and the full-wave numerical simulations (Figure 5c).

Even though the far-field absorbance remains high for all parameter values where the critical coupling condition is satisfied, our experimental results for the TiO_2-M metasurface with medium defect concentration clearly showed reduced catalytic activity compared to the TiO_2-L metasurface. To resolve this apparent discrepancy, we additionally simulate the electric near-field amplitudes (normalized to the incident electric field) around the resonant metasurface elements for varying k and θ (Figure 5d). As predicted from our theory, the parameter combinations where critical coupling occurs are identical to the far-field absorbance case. However, we observe a strong decrease of the near-field amplitudes with increasing extinction coefficient (Figure 5d, bottom), which matches the reduced reduction rates for TiO_2-M in our experiments. This behavior can be explained by the greatly increased light−matter coupling efficiency provided by the enhanced near-fields.[56] Crucially, the effects of resonant absorption for low-loss materials outweigh the benefits of higher intrinsic material losses and simultaneously deliver flexible spectral and spatial control over the absorption. This may provide the alternative way to tackle the intrinsic low absorption in the optical regime of many semiconductor materials that could be tested for sunlight driven photocatalysis. Also, it points to the nanoscale spatial locations in which cocatalysts should be located to maximize light−matter interactions.

Comparing Figures 5d and 4c, we find that the trends agree qualitatively for both defect concentrations TiO_2-L and TiO_2-M. To provide a more quantitative perspective, we combine eqs 2 and 3 to define an effective Ag coverage ratio (ECR) based on the relative deviation of the sum of pixel intensities $R_{\theta,k}$ in our dark-field images from the unenhanced case (compare, e.g., Figure 4b), which is related to the overall photocatalytic reduction rate and is given by

$$\mathrm{ECR}(\theta, k) = \frac{R_{\theta,k} - R_{\theta=0,k}}{R_{\theta=0,k}} = \beta(k)\cdot|E/E_0|^2(\theta, k) \quad (4)$$

Experimentally, the reduction of silver ions can be further confirmed through SEM (Figure 5e).

We first fix the parameters γ_{rad} and γ_{int} of the electric field enhancement $|E/E_0|^2(\theta, k)$ by fitting eq S9 with $\beta(k) = 1$ (see the Supporting Information) to numerical simulations and then fit eq 4 to the rescaled experimental data via a scaling approach, by varying β, which yields $\beta(k = 0.003) = 39 \pm 1$ for the TiO_2-L material and $\beta(k = 0.022) = 24 \pm 2$ for the TiO_2-M material (Figure 5f).

The excellent agreement of the fit further supports the importance of resonant-enhanced light−matter interaction in photocatalytic processes. While the enhancement of the ECR is mainly governed by the 6-fold increase of electric near-field intensity, β increases by 63% when comparing TiO_2-M with TiO_2-L. This highlights that the reduction rate does not scale linearly with electric near-field intensity, but rather it favors low defect concentrations even more strongly. The functional dependence of $\beta(k)$ has the potential to give insights into the reduction reaction mechanism and will be the subject of further research.

Overall, the results of this analysis offer a clear design strategy for highly efficient catalytic metasurfaces. The precise determination of scaling behavior and power dependence of the reaction is highly dependent on the exact reaction conditions, the surface structure of the materials, and the determination of the concentration of reaction products. Nevertheless, our BIC-enabled critical coupling approach provides a general framework for maximizing light−matter interactions in diverse materials, enabling us to tackle the challenges faced by many semiconductor-based ultrathin films applied in photocatalysis, such as poor light confinement and limited absorption manipulation.

CONCLUSION

In this research, based on TiO_{2-x} materials with controllable extinction coefficients, we have designed ultrathin semiconductor metasurfaces leveraging BICs to demonstrate enhancements of visible light absorption with spectral tunability and selectivity. Our multimethod analysis shows that visible-light absorption in catalytic metasurfaces can be precisely tuned for maximum enhancement through the radiative loss engineering characteristics of the BIC concept, leveraging the in-plane asymmetry of the individual unit cells to reach a critical coupling regime with balanced rates of radiative and material loss. Ultrahigh values of BIC-assisted electric field enhancement and strong light confinement have been achieved, and these were shown to produce optimal light absorption for the TiO_{2-x} film with the lowest defect concentration and therefore extinction coefficient. This provides an alternative way for tuning absorption in the optical regime in a broad range of materials. Furthermore, we demonstrated that the BIC-enabled resonant absorption can be tailored for any desired spectral position throughout the whole visible wavelength range by finely tuning the scaling factor of the metasurface unit cell. Importantly, as a versatile catalytic platform, we explore opportunities of these ultrathin TiO_{2-x}-based BIC metasurfaces for visible light photocatalysis.

https://doi.org/10.1021/acsnano.2c05680
ACS Nano 2022, 16, 13057−13068

Typically, semiconductors with high extinction coefficient k are preferred in the field of photocatalysis due to their overall higher intrinsic absorption. Our catalytic metasurface platform challenges this preconception by showing optimum resonantly enhanced light absorption for TiO_{2-x} with low k, which enables more freedom for optical engineering of the metasurface, and achieves a stronger field enhancement which makes the light−matter interaction much more intense. Finally, our catalytic TiO_{2-x}-based BIC metasurface platform enables us to circumvent long-standing drawbacks of many semiconductor-based ultrathin films applied in catalytic processes, such as poor light confinement and limited absorption manipulation, and has potential in other fields including solar-to-electric energy conversion, where our approach can help to address the long-standing trade-off in photovoltaics between optical absorption and thickness of the active layer.

METHODS

Numerical Simulations. Simulations were carried out using the finite-element frequency-domain Maxwell solver included in CST Studio Suite 2020. Experimentally measured optical constants obtained through ellipsometry were implemented for TiO_2 and TiO_{2-x} to improve the agreement between simulations and experiments. For the SiO_2 substrate, we utilize the default value (n = 1.5) implemented in CST Microwave Studio. Reflectance and transmittance spectra were simulated under linearly polarized, normally incident illumination, and the optical far-field absorbance was subsequently calculated via $A = 1 - T - R$. For monitoring the electric near-fields, a field monitor was put at the apex of the ellipse close to the substrate, where the region of maximum electric field enhancement is found.

Metasurface Fabrication. ALD was applied to produce TiO_{2-x} films (thickness 100 nm) with different defect concentrations on SiO_2 substrates. The oxygen vacancy concentration was adjusted in the deposition process using different precursors and process parameters. For our experiments, we prepared TiO_{2-x} films with three different oxygen vacancy concentrations and tailored extinction coefficients (k). The TiO_{2-x} film with the lowest oxygen vacancy concentration was prepared through plasma-enhanced ALD (PE-ALD) with the precursor tetrakis(dimethylamino) titanium (TDMAT, 99.999%, Sigma-Aldrich, kept at 75 °C), and remote oxygen plasma (300W, 99.9999%, Linde). Ar (99.9999%, Linde) was used as the purge and carrier gas creating a background pressure of 0.1 mbar throughout the process. The TiO_{2-x} films with moderate and highest oxygen vacancy concentrations were prepared through thermal ALD with precursors of titanium isopropoxide (TTIP, 99.999%, Sigma-Aldrich, kept at 65 °C) and TDMAT, respectively, using water as the oxidant. The background pressures were 0.2 and 0.3 mbar for the processes with TTIP and TDMAT. All films were deposited in a hot-wall reactor (Fiji G2, Veeco) at a substrate temperature of 200 °C. The metasurface arrays array are designed with a size of 50 × 50 unit cells, which is more than enough to ensure that the observed BIC modes correspond to the infinitely periodic array case from our simulations.[68,69] For the lithography step, the sample was first spin-coated with a layer of photoresist (PMMA 950 K A4) followed by a conducting layer (ESpacer 300Z). The two-ellipses BIC unit cell design was patterned using electron-beam lithography (Reith Eline Plus) with an acceleration voltage of 30 kV and a 15 μm aperture. The sample was transferred to a 3:1 MIBK:IPA solution to develop for 135 s, followed by deposition of a 50 nm chrome layer as the hard mask. Lift-off was conducted in Microposit Remover 1165 overnight at 80 °C, followed by reactive ion dry etching in a RCP-RIE system using a SF_6/Ar plasma. Finally, the chrome layer was removed by wet etching with chromium etchant (Sigma-Aldrich).

Optical Measurements. The refractive indices and extinction coefficients of different TiO_{2-x} films were extracted from optical modeling of variable-angle spectroscopic ellipsometry data (J.A. Woollam, M2000XI-210) measured after ALD. Ellipsometry spectra were acquired over a range of 210−1690 nm and at four different angles between 65 and 80°. The SiO_2 substrate was represented by a Cauchy layer in the optical model. The TiO_2 layer was modeled by a Cody−Lorentz for TiO_2-L and by a combination of a Cody−Lorentz and a Gaussian oscillator accounting for the sub-band-gap absorption in the case of the other two films. Reflectance/transmittance measurements of the fabricated metasurface samples were carried out with a WiTec optical microscope comprising either a water-immersion objective (20×, NA = 0.5, Zeiss, Germany) or air objective (10×, NA = 0.25, Zeiss, Germany). Illumination was provided by a Thorlabs OSL2 white light source. We use $1 - T$ to characterize the spectral response of the metasurfaces in experiments rather than $1 - T - R$ used in simulations, because obtaining the absorption requires a simultaneous measurement of reflectance and transmittance in real-time, which is not feasible in our microscopy setup.

Photoreduction Experiments. Photoreduction of Ag^+ was conducted to investigate the photocatalytic performance of the TiO_{2-x} metasurface. The TiO_{2-x} metasurface was immersed in the 50 mM $AgNO_3$ aqueous solution ($AgNO_3$, 99.9999%, Sigma-Aldrich, dissolved in ultrapure water) and exposed to 633 nm CW laser (50 mW, 60s) illumination to resonantly excite the metasurface with quasi-BIC resonance near 633 nm (measured in an aqueous environment).The laser is illuminate through a water immersion objective (20×, NA = 0.5, Zeiss, Germany) with a spot size of 13 μm in diameter on the target metasurface pattern (17 × 17 μm^2), as shown in Figure S9. After radiation, the reduced Ag nanoparticles accumulated on the surface of films, which could be observed by dark-field microscopy with a water immersion objective (63×, NA = 1.0, Zeiss, Germany). Dark-field images of metasurfaces were acquired after reaction to further analyze the amount of Ag nanoparticles deposited on the surface.

Dark-Field Image Processing. To quantify the amount of Ag particles generated during the photocatalytic reaction, we implemented a statistical image processing approach based on the dark-field images captured for the different metasurface samples. Since the photocatalytic reaction was driven using a red laser (λ = 633 nm), only the red channel of the RGB images was considered. First, the red color intensities I_n for every pixel in the image was retrieved. Then, to remove the influence of background signals, a thresholding approach was applied. Specifically, working from a dark-field image acquired on the same metasurface before reaction, we calculated the average value R_0 of all red color intensities. We could then classify the subset R_i of pixels above the threshold R_0 as relevant to the catalytic reaction, and calculate the total intensity of red pixels according to

$$R_{\text{total}} = \sum_i R_i (R_i \in I_n,\ R_i > R_0) \tag{5}$$

as a measure of the total signal contributed to the dark-field images by the Ag nanoparticles on each metasurface sample.

ASSOCIATED CONTENT

Supporting Information

The Supporting Information is available free of charge at https://pubs.acs.org/doi/10.1021/acsnano.2c05680.

Simulation results of the volume loss of the metasurfaces and maximum field enhancement of metasurfaces, experimental quality factors of the metasurfaces, experimental setup for photoreduction, 1-transmittance spectra measured for metasurfaces based on TiO_2-M, derivation of TCMT equations, spectrum of relative permittivity of TiO_{2-x} (PDF)

AUTHOR INFORMATION

Corresponding Author

Andreas Tittl − *Chair in Hybrid Nanosystems, Nanoinstitute Munich, Faculty of Physics, Ludwig-Maximilians-Universität München, 80539 München, Germany;* orcid.org/0000-

https://doi.org/10.1021/acsnano.2c05680
ACS Nano 2022, 16, 13057−13068

0003-3191-7164; Email: Andreas.Tittl@physik.uni-muenchen.de

Authors

Haiyang Hu − *Chair in Hybrid Nanosystems, Nanoinstitute Munich, Faculty of Physics, Ludwig-Maximilians-Universität München, 80539 München, Germany;* orcid.org/0000-0002-6807-5872

Thomas Weber − *Chair in Hybrid Nanosystems, Nanoinstitute Munich, Faculty of Physics, Ludwig-Maximilians-Universität München, 80539 München, Germany*

Oliver Bienek − *Walter Schottky Institute and Physics Department, Technical University Munich, 85748 Garching, Germany*

Alwin Wester − *Chair in Hybrid Nanosystems, Nanoinstitute Munich, Faculty of Physics, Ludwig-Maximilians-Universität München, 80539 München, Germany*

Ludwig Hüttenhofer − *Chair in Hybrid Nanosystems, Nanoinstitute Munich, Faculty of Physics, Ludwig-Maximilians-Universität München, 80539 München, Germany;* orcid.org/0000-0002-9507-5237

Ian D. Sharp − *Walter Schottky Institute and Physics Department, Technical University Munich, 85748 Garching, Germany;* orcid.org/0000-0001-5238-7487

Stefan A. Maier − *Chair in Hybrid Nanosystems, Nanoinstitute Munich, Faculty of Physics, Ludwig-Maximilians-Universität München, 80539 München, Germany; School of Physics and Astronomy, Monash University Clayton Campus, Melbourne, Victoria 3800, Australia; The Blackett Laboratory, Department of Physics, Imperial College London, London SW7 2AZ, United Kingdom;* orcid.org/0000-0001-9704-7902

Emiliano Cortés − *Chair in Hybrid Nanosystems, Nanoinstitute Munich, Faculty of Physics, Ludwig-Maximilians-Universität München, 80539 München, Germany;* orcid.org/0000-0001-8248-4165

Complete contact information is available at: https://pubs.acs.org/10.1021/acsnano.2c05680

Notes

The authors declare no competing financial interest.

ACKNOWLEDGMENTS

This work was funded by the Deutsche Forschungsgemeinschaft (DFG, German Research Foundation) under grant numbers EXC 2089/1−390776260 (Germany's Excellence Strategy) and TI 1063/1 (Emmy Noether Program), ERC-STG 802989 Catalight, the Bavarian program Solar Energies Go Hybrid (SolTech) and the Center for NanoScience (CeNS). S.A.M. additionally acknowledges the Lee-Lucas Chair in Physics and the EPSRC (EP/W017075/1). I.D.S. and O.B. acknowledge support by the Federal Ministry of Education and Research (BMBF, Germany) project number 033RC021B within the CO_2−WIN initiative.

REFERENCES

(1) Song, H.; Guo, L.; Liu, Z.; Liu, K.; Zeng, X.; Ji, D.; Zhang, N.; Hu, H.; Jiang, S.; Gan, Q. Nanocavity Enhancement For Ultra-Thin Film Optical Absorber. *Adv. Mater.* **2014**, *26*, 2737−2743.

(2) Kim, S. J.; Fan, P.; Kang, J. H.; Brongersma, M. L. Creating Semiconductor Metafilms With Designer Absorption Spectra. *Nat. Commun.* **2015**, *6*, 7591.

(3) Michel, J.; Liu, J.; Kimerling, L. C. High-Performance Ge-On-Si Photodetectors. *Nat. Photonics* **2010**, *4*, 527−534.

(4) Gan, Q.; Bartoli, F. J.; Kafafi, Z. H. Plasmonic-enhanced Organic Photovoltaics: Breaking The 10% Efficiency Barrier. *Adv. Mater.* **2013**, *25*, 2385−2396.

(5) Yu, Z.; Raman, A.; Fan, S. Fundamental Limit Of Nanophotonic Light Trapping In Solar Cells. *Proc. Natl. Acad. Sci. U. S. A.* **2010**, *107*, 17491−17496.

(6) Linic, S.; Christopher, P.; Ingram, D. B. Plasmonic-metal Nanostructures For Efficient Conversion Of Solar To Chemical Energy. *Nat. Mater.* **2011**, *10*, 911−921.

(7) Zhang, X.; Chen, Y. L.; Liu, R. S.; Tsai, D. P. Plasmonic Photocatalysis. *Rep. Prog. Phys.* **2013**, *76*, 046401.

(8) Shin, H.; Yanik, M. F.; Fan, S.; Zia, R.; Brongersma, M. L. Omnidirectional Resonance In A Metal-Dielectric-Metal geometry. *Appl. Phys. Lett.* **2004**, *84*, 4421−4423.

(9) Kats, M. A.; Blanchard, R.; Genevet, P.; Capasso, F. Nanometre Optical Coatings Based On Strong Interference Effects In Highly Absorbing Media. *Nat. Mater.* **2013**, *12*, 20−24.

(10) Park, J.; Kang, J. H.; Vasudev, A. P.; Schoen, D. T.; Kim, H.; Hasman, E.; Brongersma, M. L. Omnidirectional Near-Unity Absorption In An Ultrathin Planar Semiconductor Layer On A Metal Substrate. *ACS Photonics* **2014**, *1*, 812−821.

(11) Hägglund, C.; Zeltzer, G.; Ruiz, R.; Thomann, I.; Lee, H. B. R.; Brongersma, M. L.; Bent, S. F. Self-Assembly Based Plasmonic Arrays Tuned By Atomic Layer Deposition For Extreme Visible Light Absorption. *Nano Lett.* **2013**, *13*, 3352−3357.

(12) Koechlin, C.; Bouchon, P.; Pardo, F.; Jaeck, J.; Lafosse, X.; Pelouard, J. L.; Haïdar, R. Total Routing And Absorption Of Photons In Dual Color Plasmonic Antennas. *Appl. Phys. Lett.* **2011**, *99*, 241104.

(13) Hüttenhofer, L.; Golibrzuch, M.; Bienek, O.; Wendisch, F. J.; Lin, R.; Becherer, M.; Sharp, I. D.; Maier, S. A.; Cortés, E. Metasurface Photoelectrodes For Enhanced Solar Fuel Generation. *Adv. Energy Mater.* **2021**, *11*, 2102877.

(14) Deng, S.; Zhang, B.; Choo, P.; Smeets, P. J. M.; Odom, T. W. Plasmonic Photoelectrocatalysis In Copper−Platinum Core−Shell Nanoparticle Lattices. *Nano Lett.* **2021**, *21*, 1523−1529.

(15) Wu, Y.; Yang, W.; Fan, Y.; Song, Q.; Xiao, S. TiO_2 Metasurfaces: From Visible Planar Photonics To Photochemistry. *Sci. Adv.* **2019**, *5*, eaax0939.

(16) Wu, Z.; Li, L.; Zhou, X.; Parkin, I. P.; Zhao, X.; Liu, B. A Light-Heat Synergism In The Sub-Bandgap Photocatalytic Response Of Pristine TiO_2: A Study Of In Situ Diffusion Reflectance And Conductance. *Phys. Chem. Chem. Phys.* **2022**, *24*, 5618−5626.

(17) Sener, M. E.; Quesada-Cabrera, R.; Parkin, I. P.; Caruana, D. J. Facile Formation Of Black Titania Films Using An Atmospheric-Pressure Plasma Jet. *Green Chem.* **2022**, *24*, 2499−2505.

(18) Robatjazi, H.; Lou, M.; Clark, B. D.; Jacobson, C. R.; Swearer, D. F.; Nordlander, P.; Halas, N. J. Site-Selective Nanoreactor Deposition On Photocatalytic Al Nanocubes. *Nano Lett.* **2020**, *20*, 4550−4557.

(19) Seemala, B.; Therrien, A. J.; Lou, M.; Li, K.; Finzel, J. P.; Qi, J.; Nordlander, P.; Christopher, P. Plasmon-Mediated Catalytic O_2 Dissociation On Ag Nanostructures: Hot Electrons Or Near Fields? *ACS Energy Lett.* **2019**, *4*, 1803−1809.

(20) Cortés, E.; Wendisch, F. J.; Sortino, L.; Mancini, A.; Ezendam, S.; Saris, S.; de S. Menezes, L.; Tittl, A.; Ren, H.; Maier, S. A. Optical Metasurfaces for Energy Conversion. *Chem. Rev.* **2022**, DOI: 10.1021/acs.chemrev.2c00078.

(21) Hsu, C. W.; Zhen, B.; Stone, A. D.; Joannopoulos, J. D.; Soljačić, M. Bound States In The Continuum. *Nat. Rev. Mater.* **2016**, *1*, 16048.

(22) Chen, H. T.; Taylor, A. J.; Yu, N. A Review Of Metasurfaces: Physics And Applications. *Rep. Prog. Phys.* **2016**, *79*, 076401.

(23) Joseph, S.; Sarkar, S.; Khan, S.; Joseph, J. Exploring The Optical Bound State In The Continuum In A Dielectric Grating Coupled Plasmonic Hybrid System. *Adv. Opt. Mater.* **2021**, *9*, 2001895.

(24) Johnson, C. W.; Launey, K. D.; Auerbach, N.; Bacca, S.; Barrett, B. R.; Brune, C. R.; Caprio, M. A.; Descouvemont, P.; Dickhoff, W. H.; Elster, C.; et al. White Paper: From Bound States To The Continuum. *J. Phys. G Nucl. Part. Phys.* **2020**, *47*, 123001.
(25) Chen, X.; Fan, W. Tunable Bound States In The Continuum In All-Dielectric Terahertz Metasurfaces. *Nanomater.* **2020**, *10*, 623.
(26) Koshelev, K.; Lepeshov, S.; Liu, M.; Bogdanov, A.; Kivshar, Y. Asymmetric Metasurfaces With High-Q Resonances Governed By Bound States In The Continuum. *Phys. Rev. Lett.* **2018**, *121*, 193903.
(27) Melik-Gaykazyan, E.; Koshelev, K.; Choi, J. H.; Kruk, S. S.; Bogdanov, A.; Park, H. G.; Kivshar, Y. From Fano To Quasi-BIC Resonances In Individual Dielectric Nanoantennas. *Nano Lett.* **2021**, *21*, 1765−1771.
(28) Huang, J.; Liu, C.; Zhu, Y.; Masala, S.; Alarousu, E.; Han, Y.; Fratalocchi, A. Harnessing Structural Darkness In The Visible And Infrared Wavelengths For A New Source Of Light. *Nat. Nanotechnol.* **2016**, *11*, 60−66.
(29) Liu, C.; Di Falco, A.; Molinari, D.; Khan, Y.; Ooi, B. S.; Krauss, T. F.; Fratalocchi, A. Enhanced energy storage in chaotic optical resonators. *Nat. Photonics* **2013**, *7*, 473−478.
(30) Kodigala, A.; Lepetit, T.; Gu, Q.; Bahari, B.; Fainman, Y.; Kanté, B. Lasing Action From Photonic Bound States In Continuum. *Nature* **2017**, *541*, 196−199.
(31) Ha, S. T.; Fu, Y. H.; Emani, N. K.; Pan, Z.; Bakker, R. M.; Paniagua-Domínguez, R.; Kuznetsov, A. I. Directional Lasing In Resonant Semiconductor Nanoantenna Arrays. *Nat. Nanotechnol.* **2018**, *13*, 1042−1047.
(32) Mylnikov, V.; Ha, S. T.; Pan, Z.; Valuckas, V.; Paniagua-Domínguez, R.; Demir, H. V.; Kuznetsov, A. I. Lasing Action In Single Subwavelength Particles Supporting Supercavity Modes. *ACS Nano* **2020**, *14*, 7338−7346.
(33) Wu, M.; Ha, S. T.; Shendre, S.; Durmusoglu, E. G.; Koh, W. K.; Abujetas, D. R.; Sánchez-Gil, J. A.; Paniagua-Domínguez, R.; Demir, H. V.; Kuznetsov, A. I. Room-Temperature Lasing In Colloidal Nanoplatelets Via Mie-Resonant Bound States in the Continuum. *Nano Lett.* **2020**, *20*, 6005−6011.
(34) Kravtsov, V.; Khestanova, E.; Benimetskiy, F. A.; Ivanova, T.; Samusev, A. K.; Sinev, I. S.; Pidgayko, D.; Mozharov, A. M.; Mukhin, I. S.; Lozhkin, M. S.; et al. Nonlinear Polaritons In A Monolayer Semiconductor Coupled To Optical Bound States In The Continuum. *Light Sci. Appl.* **2020**, *9*, 56.
(35) Fernandez-Bravo, A.; Wang, D.; Barnard, E. S.; Teitelboim, A.; Tajon, C.; Guan, J.; Schatz, G. C.; Cohen, B. E.; Chan, E. M.; Schuck, P. J.; Odom, T. W. Ultralow-Threshold, Continuous-Wave Upconverting Lasing From Subwavelength Plasmons. *Nat. Mater.* **2019**, *18*, 1172−1176.
(36) Wang, D.; Bourgeois, M. R.; Lee, W. K.; Li, R.; Trivedi, D.; Knudson, M. P.; Wang, W.; Schatz, G. C.; Odom, T. W. Stretchable Nanolasing From Hybrid Quadrupole Plasmons. *Nano Lett.* **2018**, *18*, 4549−4555.
(37) Wang, J.; Kühne, J.; Karamanos, T.; Rockstuhl, C.; Maier, S. A.; Tittl, A. All-Dielectric Crescent Metasurface Sensor Driven by Bound States In the Continuum. *Adv. Funct. Mater.* **2021**, *31*, 2104652.
(38) Tittl, A.; John-Herpin, A.; Leitis, A.; Arvelo, E. R.; Altug, H. Metasurface-Based Molecular Biosensing Aided By Artificial Intelligence. *Angew. Chem.* **2019**, *58*, 14810−14822.
(39) Yesilkoy, F.; Arvelo, E. R.; Jahani, Y.; Liu, M.; Tittl, A.; Cevher, V.; Kivshar, Y.; Altug, H. Ultrasensitive Hyperspectral Imaging And Biodetection Enabled By Dielectric Metasurfaces. *Nat. Photonics* **2019**, *13*, 390−396.
(40) Tittl, A.; Leitis, A.; Liu, M.; Yesilkoy, F.; Choi, D.; Neshev, D. N.; Kivshar, Y. S.; Altug, H. Imaging-Based Molecular Barcoding With Pixelated Dielectric Metasurfaces. *Science.* **2018**, *360*, 1105−1109.
(41) Carletti, L.; Koshelev, K.; De Angelis, C.; Kivshar, Y. Giant Nonlinear Response At The Nanoscale Driven By Bound States In The Continuum. *Phys. Rev. Lett.* **2018**, *121*, 033903.
(42) Liu, Z.; Xu, Y.; Lin, Y.; Xiang, J.; Feng, T.; Cao, Q.; Li, J.; Lan, S.; Liu, J. High- Q Quasibound States In The Continuum For Nonlinear Metasurfaces. *Phys. Rev. Lett.* **2019**, *123*, 253901.
(43) Koshelev, K.; Tang, Y.; Li, K.; Choi, D. Y.; Li, G.; Kivshar, Y. Nonlinear Metasurfaces Governed By Bound States In The Continuum. *ACS Photonics* **2019**, *6*, 1639−1644.
(44) Koshelev, K.; Kruk, S.; Melik-Gaykazyan, E.; Choi, J.-H.; Bogdanov, A.; Park, H.-G.; Kivshar, Y. Subwavelength Dielectric Resonators For Nonlinear Nanophotonics. H. Park, Y. Kivshar. *Science* **2020**, *367*, 288−292.
(45) Ovcharenko, A. I.; Blanchard, C.; Hugonin, J. P.; Sauvan, C. Bound States In The Continuum In Symmetric And Asymmetric Photonic Crystal Slabs. *Phys. Rev. B* **2020**, *101*, 155303.
(46) Kupriianov, A. S.; Xu, Y.; Sayanskiy, A.; Dmitriev, V.; Kivshar, Y. S.; Tuz, V. R. Metasurface Engineering Through Bound States In The Continuum. *Phys. Rev. Appl.* **2019**, *12*, 014024.
(47) Bernhardt, N.; Koshelev, K.; White, S. J. U.; Meng, K. W. C.; Froch, J. E.; Kim, S.; Tran, T. T.; Choi, D. Y.; Kivshar, Y.; Solntsev, A. S. Quasi-BIC Resonant Enhancement Of Second-Harmonic Generation In WS_2 Monolayers. *Nano Lett.* **2020**, *20*, 5309−5314.
(48) Zhou, C.; Pu, T.; Huang, J.; Fan, M.; Huang, L. Manipulating Optical Scattering Of Quasi-BIC In Dielectric Metasurface With Off-Center Hole. *Nanomaterials* **2022**, *12*, 54.
(49) Tian, J.; Li, Q.; Belov, P. A.; Sinha, R. K.; Qian, W.; Qiu, M. High-Q All-Dielectric Metasurface: Super And Suppressed Optical Absorption. *Acs Photonics* **2020**, *7*, 1436−1443.
(50) Nakata, K.; Fujishima, A. TiO_2 Photocatalysis: Design And Applications. *J. Photochem. Photobiol. C Photochem. Rev.* **2012**, *13*, 169−189.
(51) Noman, M. T.; Ashraf, M. A.; Ali, A. Synthesis And Applications Of Nano-TiO_2: A Review. *Environ. Sci. Pollut. Res.* **2019**, *26*, 3262−3291.
(52) Hüttenhofer, L.; Eckmann, F.; Lauri, A.; Cambiasso, J.; Pensa, E.; Li, Y.; Cortés, E.; Sharp, I. D.; Maier, S. A. Anapole Excitations In Oxygen Vacancy-Rich TiO_{2-x} Nanoresonators: Tuning The Absorption For Photocatalysis In The Visible. *ACS Nano* **2020**, *14*, 2456−2464.
(53) Jiang, X.; Zhang, Y.; Jiang, J.; Rong, Y.; Wang, Y.; Wu, Y.; Pan, C. Characterization Of Oxygen Vacancies Associates Within The Hydrogenated TiO_2: A Positron Annihilation Study. *J.Phys.Chem.C* **2012**, *116*, 22619−22624.
(54) Hu, H.; Lin, Y.; Hu, Y. H. Core-shell Structured TiO_2 As Highly Efficient Visible Light Photocatalyst For Dye Degradation. *Catal. Today* **2020**, *341*, 90−95.
(55) Hüttenhofer, L.; Tittl, A.; Kühner, L.; Cortés, E.; Maier, S. A. Anapole-Assisted Absorption Engineering In Arrays Of Coupled Amorphous Gallium Phosphide Nanodisks. *ACS Photonics* **2021**, *8*, 1469−1476.
(56) Glass, D.; Quesada-Cabrera, R.; Bardey, S.; Promdet, P.; Sapienza, R.; Keller, V.; Maier, S. A.; Caps, V.; Parkin, I. P.; Cortés, E. Probing The Role Of Atomic Defects In Photocatalytic Systems Through Photoinduced Enhanced Raman Scattering. *ACS Energy Lett.* **2021**, *6*, 4273−4281.
(57) Kühne, J.; Wang, J.; Weber, T.; Kühner, L.; Maier, S. A.; Tittl, A. Fabrication robustness in BIC metasurfaces. *Nanophotonics* **2021**, *10*, 4305−4312.
(58) Adato, R.; Artar, A.; Erramilli, S.; Altug, H. Engineered Absorption Enhancement And Induced Transparency In Coupled Molecular And Plasmonic Resonator Systems. *Nano Lett.* **2013**, *13*, 2584−2591.
(59) Piper, J. R.; Liu, V.; Fan, S. Total Absorption By degenerate Critical Coupling. *Appl. Phys. Lett.* **2014**, *104*, 251110.
(60) Glass, D.; Cortés, E.; Ben-Jaber, S.; Brick, T.; Peveler, W. J.; Blackman, C. S.; Howle, C. R.; Quesada-Cabrera, R.; Parkin, I. P.; Maier, S. A. Dynamics Of Photo-Induced Surface Oxygen Vacancies In Metal-Oxide Semiconductors Studied Under Ambient Conditions. *Adv. Sci.* **2019**, *6*, 1901841.
(61) Dagdeviren, O. E.; Glass, D.; Sapienza, R.; Cortés, E.; Maier, S. A.; Parkin, I. P.; Grütter, P.; Quesada-Cabrera, R. The Effect Of Photoinduced Surface Oxygen Vacancies On The Charge Carrier Dynamics in TiO_2 Films. *Nano Lett.* **2021**, *21*, 8348−8354.

https://doi.org/10.1021/acsnano.2c05680
ACS Nano 2022, 16, 13057−13068

(62) Naldoni, A.; Altomare, M.; Zoppellaro, G.; Liu, N.; Kment, Š.; Zbořil, R.; Schmuki, P. Photocatalysis With Reduced TiO_2: From Black TiO_2 to Cocatalyst-Free Hydrogen Production. *ACS Catal.* **2019**, *9*, 345−364.
(63) Pan, X.; Yang, M. Q.; Fu, X.; Zhang, N.; Xu, Y. J. Defective TiO_2 with oxygen vacancies: synthesis, properties and photocatalytic applications. *Nanoscale* **2013**, *5*, 3601−3614.
(64) Fujishima, A.; Zhang, X.; Tryk, D. A. TiO_2 photocatalysis and related surface phenomena. *Surf. Sci. Rep.* **2008**, *63*, 515−582.
(65) Fan, S.; Suh, W.; Joannopoulos, J. D. Temporal Coupled-Mode Theory For The Fano Resonance In Optical Resonators. *JOSA A* **2003**, *20*, 569−572.
(66) Suh, W.; Wang, Z.; Fan, S. Temporal Coupled-Mode Theory And The Presence Of Non-Orthogonal Modes In Lossless Multimode Cavities. *IEEE J. Quantum Electron.* **2004**, *40*, 1511−1518.
(67) Hou, W.; Cronin, S. B. A Review Of Surface Plasmon Resonance-Enhanced Photocatalysis. *Adv. Funct. Mater.* **2013**, *23*, 1612−1619.
(68) Koshelev, K.; Kruk, S.; Melik-gaykazyan, E.; Choi, J.; Bogdanov, A.; Park, H.; Kivshar, Y. Subwavelength dielectric resonators for nonlinear nanophotonics. *Science* **2020**, *367*, 288−292.
(69) Büchner, R.; Weber, T.; Kühner, L.; Maier, S. A.; Tittl, A. Tip Coupling and Array Effects of Gold Nanoantennas in Near-Field Microscopy. *ACS Photonics* **2021**, *8*, 3486−3494.

https://doi.org/10.1021/acsnano.2c05680
ACS Nano 2022, 16, 13057−13068